nature geoscience

ARTICLES

https://doi.org/10.1038/s41561-020-0637-7

Global nitrous acid emissions and levels of regional oxidants enhanced by wildfires

N. Theys[1]✉, R. Volkamer[2,3,4]✉, J.-F. Müller[1], K. J. Zarzana[2], N. Kille[3,4], L. Clarisse[5], I. De Smedt[1], C. Lerot[1], H. Finkenzeller[2,3], F. Hendrick[1], T. K. Koenig[2,3], C. F. Lee[2,3], C. Knote[6], H. Yu[1] and M. Van Roozendael[1]

Nitrous acid (HONO) is a precursor of the hydroxyl radical in the atmosphere, which controls the degradation of greenhouse gases, contributes to photochemical smog and ozone production, and influences air quality. Although biomass burning is known to contribute substantially to global aerosols and reactive gas emissions, pyrogenic contributions to HONO emissions are poorly constrained and often omitted in models. Here we present a global survey of TROPOMI/Sentinel-5 Precursor satellite sounder observations and show that HONO emissions are consistently enhanced in fresh wildfire plumes. Comparing major ecosystems (savanna, grassland, shrubland and tropical and extratropical forests), we found that the enhancement ratios of HONO to nitrogen dioxide varied systematically with biome type, with the lowest in savannas and grasslands and highest in extratropical evergreen forests. Supported by airborne measurements, we demonstrate that previous assessments underestimate pyrogenic HONO emissions by a factor of 2–4 across all ecosystem types. We estimate that HONO emissions are responsible for two-thirds of the hydroxyl radical production in fresh wildfire plumes worldwide and act to accelerate oxidative plume chemistry and ozone production. Our findings suggest that pyrogenic HONO emissions have a substantial impact on atmospheric composition, which enhances regional ozone levels by up to 7 ppbv.

As the primary oxidant of the atmosphere, hydroxyl radicals (OH) control the degradation of pollutants and greenhouse gases, and contribute to photochemical smog and ozone (O_3) formation[1]. Nitrous acid (HONO) is a key constituent of the tropospheric photochemistry, primarily as a source of OH. However, the HONO budget remains poorly constrained[2], despite recent scientific progress[3–7].

Biomass burning (BB) plays an important role in the global emission budget of reactive gases in the atmosphere[8]. Fires can cause large perturbations to the chemistry and composition of the atmosphere, which affect climate and lead to adverse effects on human health. Atmospheric chemical transport models provide an ideal means to assess these impacts, but require an accurate representation of the chemistry in fire plumes as well as reliable ecosystem-dependent emission estimates that are usually based on fire activity data together with estimated emission factors obtained from laboratory and in situ measurements[9,10].

Global models that assess the importance of HONO as a OH precursor on the global scale[11] typically neglect HONO from wildfires and thus provide lower-limit estimates. The known formation mechanisms of HONO in fire plumes include direct emissions[12], heterogeneous conversion of nitrogen dioxide (NO_2) on organic aerosols[4,13] and on soot[3,14], photolysis of particulate nitrate[15] and hydrolysis of NO_2 dimers boosted in the presence of ammonia[16]. However, the relative importance of these processes in fires and on the HONO to NO_x ($NO+NO_2$) emission factors has proved difficult to quantify, especially on large scales, due to the lack of representativeness of measurements performed in smoke chambers[17,18] or collected in situ[19–24], and also because of the short atmospheric lifetime of HONO. Global satellite sounders have revolutionized our knowledge on the emission mechanisms and global distributions of many short-lived gaseous pollutants[25–27]. HONO, however, has hitherto been detected only once from space, namely, in an exceptionally large stratospheric smoke plume[28] using the Infrared Atmospheric Sounder Interferometer. Here we show that the new satellite TROPOspheric Monitoring Instrument (TROPOMI), launched in 2017 onboard Sentinel-5 Precursor, is capable of observing HONO consistently in freshly emitted wildfire plumes, which provides information that is otherwise unavailable. To achieve this, TROPOMI has two decisive advantages over its predecessors (such as the Ozone Monitoring Instrument), namely a high spatial resolution ($3.5\times7\,km^2$) and a higher signal-to-noise ratio. Compared with infrared sounders, TROPOMI measures in the ultraviolet–visible domain and has a much better sensitivity to HONO in the lowermost atmosphere.

Global pyrogenic HONO probed from space

Daily global HONO slant column densities (SCD, or the integrated concentration along the light path) were retrieved from TROPOMI radiance spectra (Methods) using differential optical absorption spectroscopy[29,30] (DOAS). A typical example is shown in Fig. 1a for wildfires in British Columbia, along with unambiguous spectroscopic evidence for the presence of HONO in the selected TROPOMI observation (Fig. 1a lower inset). Inspection of the daily HONO maps reveals consistent large local enhancements near the fire sources similar to enhancements of NO_2 SCD that are co-retrieved in the same wavelength range (Supplementary Fig. 1a). This suggests that HONO is either directly emitted from fires or

[1]Royal Belgian Institute for Space Aeronomy (BIRA-IASB), Brussels, Belgium. [2]Department of Chemistry, University of Colorado Boulder, Boulder, CO, USA. [3]Cooperative Institute for Research in Environmental Sciences (CIRES), Boulder, CO, USA. [4]Department of Atmospheric Sciences, University of Colorado Boulder, Boulder, CO, USA. [5]Université libre de Bruxelles (ULB), Spectroscopy, Quantum Chemistry and Atmospheric Remote Sensing (SQUARES), C. P. 160/09, Brussels, Belgium. [6]Meteorological Institute, LMU Munich, Munich, Germany. ✉e-mail: theys@aeronomie.be; rainer.volkamer@colorado.edu

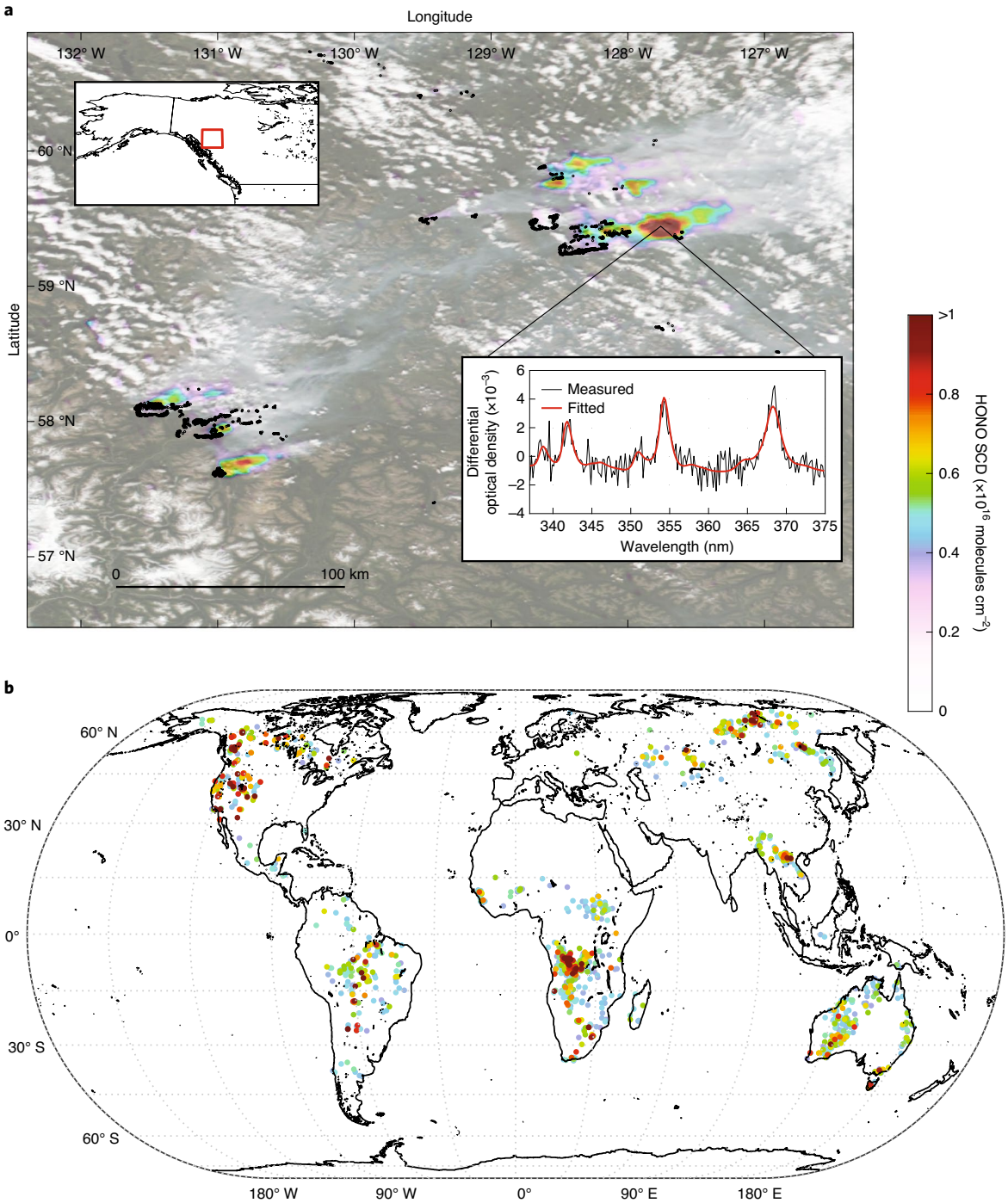

Fig. 1 | Detection of HONO in wildfire plumes by TROPOMI. a, Example map of HONO SCDs for wildfires in British Columbia on 21 August 2018. The background layer is a composite of true-colour RGB image with fire detection and thermal anomaly product (black points) from the VIIRS/Suomi-NPP instrument (https://worldview.earthdata.nasa.gov/), which shows smoke aerosols and the fire source locations. Lower inset: spectral proof of the HONO detection in the satellite pixel centred at 59.45° N, 127.82° W, which illustrates the presence of the HONO differential absorption in the measured spectrum. **b**, Global map of HONO SCD detections (Methods) for one year of TROPOMI measurements.

very rapidly formed by pyrogenic precursors. The geographical extent of the observed HONO plumes is generally limited to a few tens of kilometres downwind of the fires, which reflects the short atmospheric lifetime of HONO (around 15 minutes in clear air[31], longer in smoke plumes) and the rapidly changing conditions as the plumes age and dilute. We analysed one full year of global measurements between May 2018 and April 2019. Based on conservative selection criteria (Methods), we isolated a total of 5,093 TROPOMI pixels with unambiguous HONO detection, all of which coincided with wildfire plumes, as readily confirmed by TROPOMI-retrieved distribution of other pyrogenic compounds, which included carbon monoxide (CO), NO_2, formaldehyde (HCHO), glyoxal (CHOCHO), and aerosols (see examples in Supplementary Fig. 1). These HONO observations (Fig. 1b) are located over dominant BB regions, as

evidenced from the data of GFED (Global Fire Emissions Database[32]; Supplementary Fig. 2a), and enable assessment of HONO emissions from fires in a global context.

Comparison with aircraft observations

The TROPOMI HONO measurements are corroborated by comparisons with aircraft HONO column observations acquired during the Biomass Burning Fluxes of Trace Gases and Aerosols (BB-FLUX) field study conducted in the US Pacific Northwest during the summer of 2018 wildfire season (Methods). Here we used measurements of the wildfire plume from the Rabbit Foot Fire, Idaho, on 12 August 2018. The aircraft, equipped with a zenith-sky DOAS instrument, flew under the smoke layer and performed two traverses of the plume, nearly synchronized with TROPOMI. HONO and NO_2 were retrieved using identical fit settings as those used by the satellite. The HONO SCDs derived from the aircraft measurements provide independent corroborating evidence for the presence of HONO in large amounts at the same location as that of the satellite observations (Fig. 2a). Notably, the aircraft measurement integrated HONO and NO_2 over the entire wildfire plume, whereas the satellite measurement primarily sampled the top layer of the plume (Supplementary Fig. 3). The higher HONO SCD measured from the aircraft reflects the fact that all the photons that reach the plane have traversed the entire plume. For comparison with the satellite, we compared the enhancement ratios of the measured HONO SCD to the NO_2 SCD (RHN) to cancel differences in air mass factors (AMFs) that arise from the different sampling geometries. The RHN cancellation of AMFs is justified because both gases are retrieved in the same wavelength range (Methods), as long as the HONO and NO_2 profile shapes in the plume are similar (Supplement). Similar profile shapes are expected because both are photolabile species. Furthermore, the RHN is independent of the trace gas dilution during transport, and a useful metric[18,33] of the photochemical production rate of HONO.

Comparisons of TROPOMI and aircraft RHNs are presented in Fig. 2b,c. The satellite RHNs (0.33–0.54) agree very well with the aircraft values (0.29–0.54) when the data are aligned along a common plume age axis (Methods). There is no satellite bias discernible within the low (<10%) measurement error of the aircraft data. Two additional BB-FLUX research flights (RFs) (Extended Data Fig. 1) show similarly good agreements over a wider range of RHN values, which further supports the assumption of similar HONO and NO_2 profile shapes inside the plume. The aircraft data reveal variability in the RHN on fine spatial (a few hundred metres) and temporal scales (seconds to minutes) that cannot be resolved from space. Notably, comparing aircraft column observations with columns from space actively bridges the different spatial scales to the best degree possible, although atmospheric variability remains a limiting factor. Overall, Fig. 2c and Extended Data Fig. 1 illustrate that the aircraft data approximate the satellite-measured RHN best when near-synchronous observations of similar plume ages are compared.

Uncertainties in HONO and NO_2 SCDs and RHN

No statistically significant bias in the satellite RHN was observed ($6 \pm 8\%$; Supplementary Table 1), which reflects the identical HONO and NO_2 retrieval settings and cross-section spectra used for both aircraft and satellite (known to better 6 and 5%, respectively; Supplementary Table 1). However, a common systematic error could not be fully excluded either. For TROPOMI global observations, the RHN systematic uncertainty is $\pm 25\%$. The contribution of SCD random errors to biome-averaged RHN values (Table 1) was negligible due to the large number of HONO detections. Furthermore, the RHN variability within a satellite ground pixel was found to be highly significant in the aircraft data, and similar to the variability between nearby satellite detections (Fig. 2c and Extended Data Fig. 1). Interestingly, the satellite bias was also insignificant, within the $\pm 6.9\%$ uncertainty of the aircraft data (accuracy in RHN, excluding cross-sections errors). This suggests that plume heterogeneity did not limit the comparison between both remote sensing platforms, and reflects the benefits of a more direct comparison by sampling over extended spatial scales. The TROPOMI RHNs were also found to be in general good agreement with in situ observations from the Western Wildfire Experiment for Cloud Chemistry, Aerosol Absorption and Nitrogen campaign data[34]. Yet, the comparison is challenging due to limited synchronous data, differences in spatial–temporal sampling and instrument calibrations.

Enhanced HONO relative to NO_2 surveyed worldwide

In Fig. 2b,c, it is noteworthy that the TROPOMI RHN substantially increases (to values as high as 1.2) for pixels near the fire sources. This feature is commonly observed for fires globally, and is directly the result of elevated HONO SCDs (rather than low NO_2 SCDs) near the fires (Extended Data Fig. 2). This suggests that HONO primary emissions either dominate over secondary sources or cannot easily be separated from fast secondary formation close to the fires. From the global detections, distinct spatial patterns of RHN clearly emerge (Fig. 3a) that are attributable to the distribution of ecosystems. Observed RHNs (10th–90th percentile) tend to be lower (0.14–0.61) over regions dominated by fires from grassland, savannas and open shrubland (Kazakhstan, most of Africa and Australia), intermediate values (0.23–0.62) are found over tropical deciduous forest fires (Central and South America, mainland Southeast Asia, the eastern coast of Australia and east of Madagascar) and the highest values (0.32–0.78) correspond to extratropical evergreen forest burns (USA, Canada and far Eastern Russia). This dependence of RHN on vegetation type matches the findings of earlier studies (Table 1). However, the TROPOMI RHN is a factor of 2–4 higher compared with most values found in the current literature[10], regardless of the vegetation type. This is highly significant, and well outside the measurement uncertainty. Owing to the detection limit, satellite data are more representative of large wildfires (Supplementary Fig. 2b), but the finding of high RHNs is robust over the complete range of fire emissions covered by TROPOMI HONO measurements (Supplementary Fig. 2c). For savanna fires, a statistically significant anticorrelation between the fire strength and RHN is observed, consistent with strong savanna fires that emit larger amounts of NO_x. Our results suggest that the global HONO production from fires has been largely underestimated, and we present several reasons for this. First, the published RHN estimates from field studies (Supplementary Table 2) are based on in situ measurements, most often for modest burns, optically thin BB plumes (thus very different to the fire emissions sampled by TROPOMI and BB-FLUX) and samples away from the core of fire plumes. This is supported by recent in situ observations of high RHNs in fresh plumes from large fires[34], consistent with our global findings. Second, the highly polluted conditions in sizeable fire plumes probably favour the conversion of NO_2 into HONO through heterogeneous processes[3,13,16] as well as NO_2 loss, for instance, from peroxyacetyl nitrate formation (PAN). These effects would be seen more in the distal rather than the proximal part of the plume, so that such a potential bias can only explain part of the observed discrepancy. Third, the higher RHNs derived from TROPOMI observations probably reflect the ability to sample freshly emitted, almost undiluted plumes inside the zone surrounding the fires that is hardly accessible to RFs, because of fire-induced atmospheric turbulence and/or due to temporary flight restriction zones. A clear decrease is observed for RHN, HONO and NO_2 with increasing distance from the fires (Extended Data Fig. 2). This presents direct evidence for the difficulty of establishing emission factors for highly reactive species from field measurements downwind of fires in rapidly evolving plumes, whose composition changes on short temporal and spatial scales. Fourth, emission factors determined from smoke chamber experiments

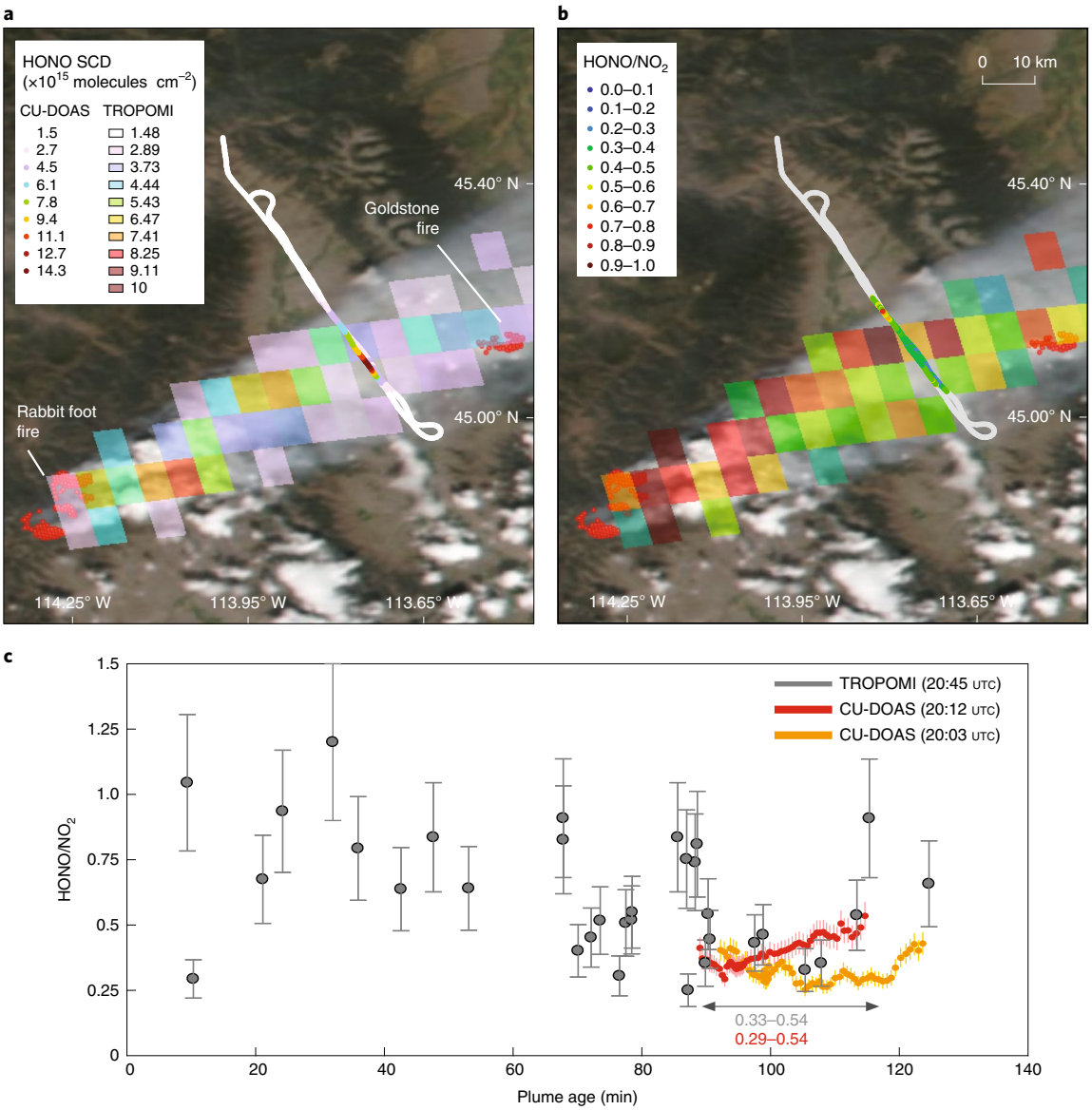

Fig. 2 | Comparison between TROPOMI and aircraft (CU-DOAS) measurements of the Rabbit Foot Fire on 12 August 2018. a, HONO slant columns from TROPOMI (rectangles) and aircraft CU-DOAS (dots). The colour scales best represent the ranges of observed values. **b**, RHN for measurements with unambiguous detection of HONO and NO_2. The background images for **a** and **b** show BB aerosols and the fire source locations (same data source as for Fig. 1a). **c**, Comparison between TROPOMI and aircraft RHN as a function of plume age (Methods). The two aircraft traverses of the plume are plotted separately. The ranges of RHN from TROPOMI and CU-DOAS are given over the intersection plume age interval (double arrow), for the traverse closest in time to the satellite. Error bars correspond to systematic uncertainties on RHNs.

Table 1 | RHNs reported in the literature (Supplementary Table 2) and in this study for different types of BB

	Savanna, grassland, shrubland	Tropical forest	Extratropical forest
Field measurements	0.05–0.10	0.17–0.22	0.06–0.41 (0.86[a])
Laboratory experiments	0.05–0.19	0.17	0.13–0.20
This study[b] (average ± error[c])	0.34 ± 0.08	0.41 ± 0.09	0.54 ± 0.12

The TROPOMI results are classified using MODIS land cover type[39]. [a]Fresh smoke from large wildfires[34]. [b]Mean values for satellite HONO detections, mostly representative of fires with carbon emissions of 0.5–500 gC m^{-2} $month^{-1}$ (Supplementary Fig. 2b). [c]Systematic uncertainty.

(Table 1) are obtained under specific atmospheric mixing and photochemical conditions that prevail in the laboratory settings, and that are probably different from the conditions found in actual wildfires (in terms of fuel heterogeneity, wind fields, humidity gradients, fire strength, fuel consumption rates, pyrolysis contributions and so on). Consistent with this hypothesis, our evidence that RHN depends on the fire strength of savanna fires (Supplementary Fig. 2c) corroborates previous findings[35] that burn conditions modify fire emissions.

HONO as the main source of OH in fresh smoke plumes

The importance of HONO for atmospheric chemistry in fire plumes is further demonstrated by contrasting the calculated production rates of OH due to HONO photolysis with the corresponding estimated production rates due to other known pyrogenic sources of

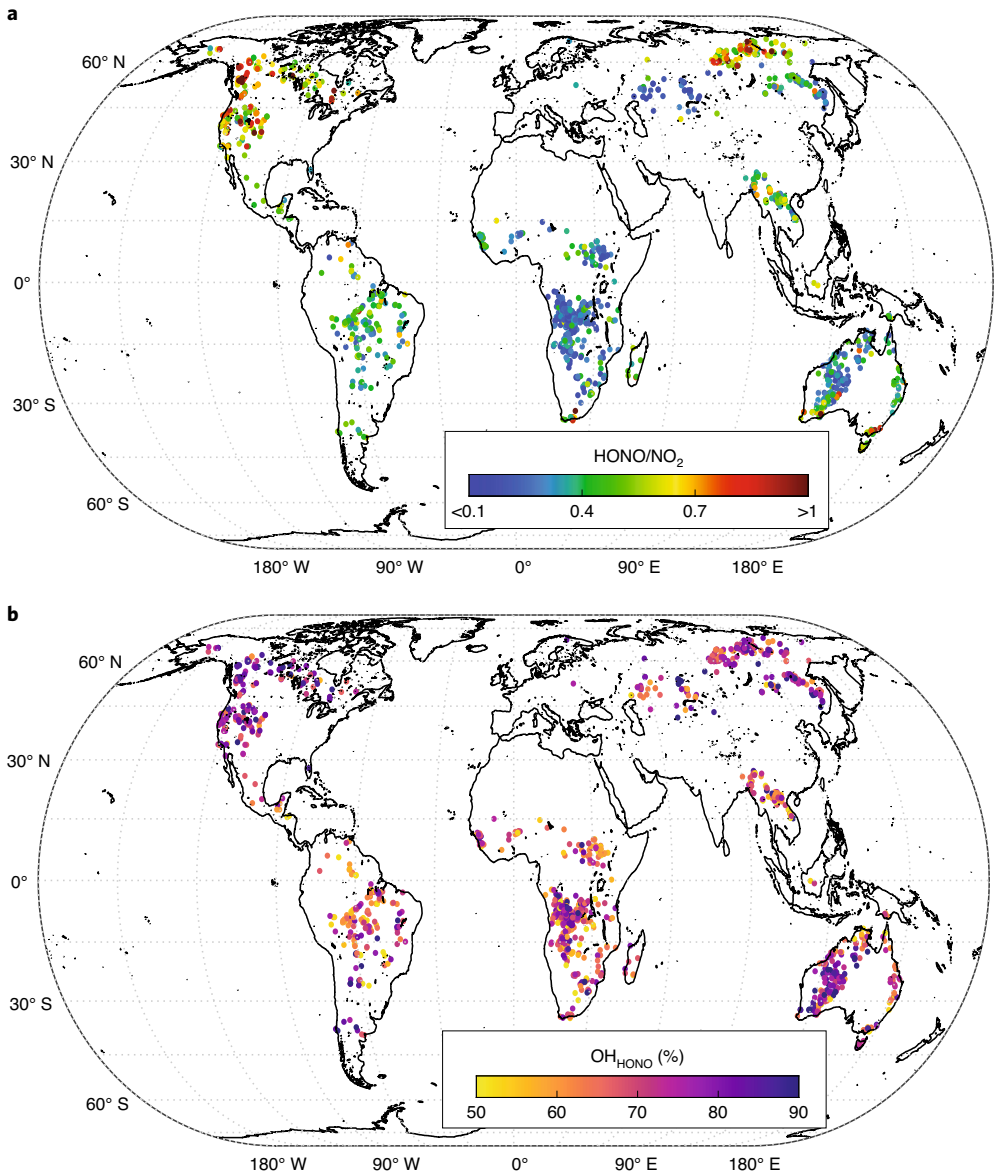

Fig. 3 | Satellite-derived RHNs and relative production rates of OH due to HONO photolysis for fire emissions. a, RHNs for one year of TROPOMI measurements (May 2018 to April 2019). The coloured symbols correspond to individual HONO detections (as in Fig. 1b). **b**, Satellite estimates of OH production from HONO fire emissions. The OH production is calculated from HONO concentrations derived from the satellite detections (as in **a**), assuming a single AMF and a fixed HONO concentration profile shape (Methods).

OH, which include the photolysis of O_3 in the presence of H_2O, the photolysis of 16 oxygenated volatile organic compounds (VOCs) and the ozonolysis of 12 alkenes (Methods). Constrained by TROPOMI measurements, we estimate the relative contributions of the most important precursory compounds to the total OH production in fresh wildfire plumes worldwide, leveraging the fact that relative contributions are independent of assumptions about aerosol optical properties and plume optical thickness to the first order (Methods). On average for all the wildfire plumes detected by TROPOMI, the photolysis of HONO accounts for $63 \pm 16\%$ of the total OH production, and more than 80% locally (Fig. 3b); the error range accounts for uncertainties in the abundances of the contributing compounds and in their lower rates and OH yields. The photolysis of all the oxygenated VOCs accounts collectively for 34% (HCHO, 18%; CHOCHO, 4%; other oxygenated VOCs, 12%), and other sources for 3% (O_3 photolysis, 1%; alkenes ozonolysis, 2%) of the total OH production from fires. The daytime contribution of HONO obtained here is much higher than previously reported (12–34%), for urban conditions[36,37] and forest canopy[38]. This makes HONO the main precursor of OH in fresh fire plumes; this finding is supported on a local scale by the reported large OH production due to HONO from western US wildfires[34]. Under the simplifying assumption that pyrogenic HONO is directly emitted, its impact on other atmospheric compounds is also substantial. We estimate concentration enhancements of up to 30% for OH and 10% for O_3 with global model simulations (Extended Data Fig. 3). Pyrogenic HONO emissions also represent a notable input to the global NO_x budget, estimated at ~1 TgN yr^{-1}.

This work demonstrates that HONO emissions can be assessed at a global scale using observations from space. The detailed study of further HONO observations—which include from geostationary platforms—in connection with models and additional atmospheric

and fire activity data holds a largely unexplored potential to provide valuable insights into the still poorly understood formation mechanisms of HONO, and its importance for atmospheric chemistry and climate in the global context of wildfires, and possibly also urban air.

Online content

Any methods, additional references, Nature Research reporting summaries, source data, extended data, supplementary information, acknowledgements, peer review information; details of author contributions and competing interests; and statements of data and code availability are available at https://doi.org/10.1038/s41561-020-0637-7.

Received: 24 February 2020; Accepted: 20 August 2020;
Published online: 21 September 2020

References

1. Finlayson-Pitts, B. J. & Pitts, J. N. *Chemistry of the Upper and Lower Atmosphere: Theory, Experiments and Applications* (Academic, 2000).
2. Spataro, F. & Ianniello, A. Sources of atmospheric nitrous acid: state of the science, current research needs, and future prospects. *J. Air Waste Manage. Assoc.* **64**, 1232–1250 (2014).
3. Ammann, M. et al. Heterogeneous production of nitrous acid on soot in polluted air masses. *Nature* **395**, 157–160 (1998).
4. Stemmler, K., Ammann, M., Donders, C., Kleffmann, J. & George, C. Photosensitized reduction of nitrogen dioxide on humic acid as a source of nitrous acid. *Nature* **440**, 195–198 (2006).
5. Zhou, X. et al. Nitric acid photolysis on forest canopy surface as a source for tropospheric nitrous acid. *Nat. Geosci.* **4**, 440–443 (2011).
6. Oswald, R. et al. HONO emissions from soil bacteria as a major source of atmospheric reactive nitrogen. *Science* **341**, 1233–1235 (2013).
7. VandenBoer, T. C. et al. Nocturnal loss and daytime source of nitrous acid through reactive uptake and displacement. *Nat. Geosci.* **8**, 55–60 (2015).
8. Andreae, M. O. & Merlet, P. Emissions of trace gases and aerosols from biomass burning. *Global Biogeochem. Cycles* **15**, 955–966 (2001).
9. Akagi, S. K. et al. Emission factors for open and domestic biomass burning for use in atmospheric models. *Atmos. Chem. Phys.* **11**, 4039–4072 (2011).
10. Andreae, M. O. Emissions of trace gases and aerosols from biomass burning—an updated assessment. *Atmos. Chem. Phys.* **19**, 8523–8546 (2019).
11. Elshorbany, Y. F. et al. Global and regional impacts of HONO on the chemical composition of clouds and aerosols. *Atmos. Chem. Phys.* **14**, 1167–1184 (2014).
12. Veres, P. et al. Measurements of gas-phase inorganic and organic acids from biomass fires by negative-ion proton-transfer chemical-ionization mass spectrometry. *J. Geophys. Res.* **115**, D23302 (2010).
13. Nie, W. et al. Influence of biomass burning plumes on HONO chemistry in eastern China. *Atmos. Chem. Phys.* **15**, 1147–1159 (2015).
14. Monge, M. E. et al. Light changes the atmospheric reactivity of soot. *Proc. Natl Acad. Sci. USA* **107**, 6605–6609 (2010).
15. Ye, C., Zhang, N., Gao, H. & Zhou, X. Photolysis of particulate nitrate as a source of HONO and NO_x. *Environ. Sci. Technol.* **51**, 6849–6856 (2017).
16. Li, L. et al. Formation of HONO from the NH_3-promoted hydrolysis of NO_2-dimers in the atmosphere. *Proc. Natl Acad. Sci. USA* **115**, 7236–7241 (2018).
17. Keene, W. C. et al. Emissions of major gaseous and particulate species during experimental burns of southern African biomass. *J. Geophys. Res.* **111**, D04301 (2006).
18. Burling, I. R. et al. Laboratory measurements of trace gas emissions from biomass burning of fuel types from the southeastern and southwestern United States. *Atmos. Chem. Phys.* **10**, 11115–11130 (2010).
19. Trentmann, J. et al. An analysis of the chemical processes in the smoke plume from a savanna fire. *J. Geophys. Res.* **110**, D12301 (2005).
20. Yokelson, R. J. et al. The tropical forest and fire emissions experiment: overview and airborne fire emission factor measurements. *Atmos. Chem. Phys.* **7**, 5175–5196 (2007).
21. Yokelson, R. J. et al. Emissions from biomass burning in the Yucatan. *Atmos. Chem. Phys.* **9**, 5785–5812 (2009).
22. Akagi, S. K. et al. Measurements of reactive trace gases and variable O_3 formation rates in some South Carolina biomass burning plumes. *Atmos. Chem. Phys.* **13**, 1141–1165 (2013).
23. Müller, M. et al. In situ measurements and modeling of reactive trace gases in a small biomass burning plume. *Atmos. Chem. Phys.* **16**, 3813–3824 (2016).
24. Neuman, J. A. et al. HONO emission and production determined from airborne measurements over the Southeast U.S. *J. Geophys. Res. Atmos.* **121**, 9237–9250 (2016).
25. Beirle, S., Boersma, K. F., Platt, U., Lawrence, M. G. & Wagner, T. Megacity emissions and lifetime of nitrogen oxides probed from space. *Science* **333**, 1737–1739 (2011).
26. McLinden, C. A. et al. Space-based detection of missing sulfur dioxide sources of global air pollution. *Nat. Geosci.* **9**, 496–500 (2016).
27. Van Damme, M. et al. Industrial and agricultural ammonia point sources exposed. *Nature* **564**, 99–103 (2018).
28. Clarisse, L., R'Honi, Y., Coheur, P.-F., Hurtmans, D. & Clerbaux, C. Thermal infrared nadir observations of 24 atmospheric gases. *Geophys. Res. Lett.* **38**, L10802 (2011).
29. Platt, U., Perner, D., Harris, G. W., Winer, A. M. & Pitts, J. N. Observations of nitrous acid in an urban atmosphere by differential optical absorption. *Nature* **285**, 312–314 (1980).
30. Platt, U. & Stutz, J. *Differential Optical Absorption Spectroscopy (DOAS), Principle and Applications* (Springer, 2008).
31. Hendrick, F. et al. Four years of ground-based MAX-DOAS observations of HONO and NO_2 in the Beijing area. *Atmos. Chem. Phys.* **14**, 765–781 (2014).
32. van der Werf, G. R. et al. Global fire emissions estimates during 1997–2016. *Earth Syst. Sci. Data* **9**, 697–720 (2017).
33. Kleffmann, J. Daytime sources of nitrous acid (HONO) in the atmospheric boundary layer. *Chem. Phys. Chem.* **8**, 1137–1144 (2007).
34. Peng, Q. et al. HONO emissions from western U.S. wildfires provide dominant radical source in fresh wildfire smoke. *Environ. Sci. Technol.* **54**, 5954–5963 (2020).
35. Liu, X. et al. Airborne measurements of western U.S. wildfire emissions: comparison with prescribed burning and air quality implications. *J. Geophys. Res. Atmos.* **112**, 6108–6129 (2017).
36. Alicke, B., Platt, U. & Stutz, J. Impact of nitrous acid photolysis on the total hydroxyl radical budget during the Limitation of Oxidant Production/Pianura Padana Produzione di Ozono study in Milan. *J. Geophys. Res. Atmos.* **107**, 8196 (2002).
37. Volkamer, R., Sheehy, P., Molina, L. T. & Molina, M. J. Oxidative capacity of the Mexico City atmosphere—Part 1: a radical source perspective. *Atmos. Chem. Phys.* **10**, 6969–2991 (2010).
38. Kleffmann, J. et al. Daytime formation of nitrous acid: a major source of OH radicals in a forest. *Geophys. Res. Lett.* **32**, L05818 (2005).
39. Friedl, M. A. et al. MODIS Collection 5 global land cover: algorithm refinements and characterization of new datasets. *Remote Sens. Environ.* **114**, 168–182 (2010).

Methods

TROPOMI retrieval of HONO and NO_2. TROPOMI[40] is the single payload of the Sentinel-5 Precursor platform launched in October 2017. It is a nadir-viewing remote sensing instrument that measures the solar radiation reflected by the Earth and backscattered by its atmosphere. TROPOMI has heritage from the Ozone Monitoring Instrument[41] and the scanning imaging absorption spectrometer for atmospheric cartography[42] (SCIAMACHY). The instrument is a push-broom imaging spectrometer that covers ultraviolet to shortwave infrared wavelengths with a spectral resolution of 0.25–1 nm. It flies in a low-Earth early afternoon polar orbit with a wide swath of 2,600 km, which results in a daily global coverage. It delivers vertically integrated abundances of key atmospheric constituents (O_3, NO_2, SO_2, HCHO, CHOCHO, CO and methane) complemented by cloud and aerosol information at a resolution of $3.5\times5.5\,km^2$ (from 6 August 2019) or $3.5\times7\,km^2$ (this study, compared with $13\times24\,km^2$ and $30\times60\,km^2$ for the Ozone Monitoring Instrument and SCIAMACHY, respectively).

We analysed ultraviolet–visible spectral data measured between 1 May 2018 and 30 April 2019, and solar zenith angles lower than 65°. The HONO SCD (molecules cm^{-2}) was retrieved from each recorded radiance spectrum using the established technique of DOAS[30]. In brief, the measured spectrum was modelled using a reference spectrum, absorption cross-sections of relevant trace gases and radiance closure terms. The fitted parameters for the trace gases were the SCDs and represent the corresponding concentrations integrated along the mean optical light path in the atmosphere. Here the retrieval scheme is an adapted version of the TROPOMI HCHO algorithm[43]. We followed recommended settings[44] and used a wavelength interval of 337–375 nm optimized for HONO (Supplementary Table 3). In the same spectral fitting step, the slant column of NO_2 was retrieved. Given the relatively low peak-to-peak absorption of NO_2 in the ultraviolet, the noise on the retrieved NO_2 SCDs is larger than that in the visible range[45]. However, the signal is such that it is not difficult to detect NO_2 in wildfire plumes. To determine the enhanced NO_2 SCD for the fire plumes, a stratospheric NO_2 correction was applied, estimated using measurements at the same latitude over a sector with negligible tropospheric NO_2 contribution (Supplementary Table 3)[46].

Determination of the vertical column density (VCD; vertically integrated concentration) from the measured SCD requires radiative transfer simulations to derive the AMF, where AMF = SCD/VCD. The AMF simulates the trace gas concentration integrated along the complex photon path in the plume, relative to the vertical path. Here, the AMF is formulated[47] by:

$$\mathrm{AMF} = \int \mathrm{bAMF}(z)N(z)\mathrm{d}z \qquad (1)$$

where $N(z)$ is the trace gas normalized concentration profile and bAMF is the height-resolved AMF (referred as the box-AMF) that contains all the dependences to parameters (wavelength, geometry, surface reflectance, clouds, aerosols and so on) that influence the vertical sensitivity of the measurement, except $N(z)$. In the case of HONO and NO_2 from fires, a general AMF computation applicable globally is difficult because crucial parameters are poorly known, notably the vertical distributions of trace gases and the aerosol optical properties and extinction vertical profile (which impact bAMF).

We calculated the RHN, a proxy for HONO production, independent of the dilution of the trace gases during transport. As NO_2 and HONO are jointly retrieved in the same spectral region, the box-AMFs can be considered identical for both species. Under the assumption that HONO and NO_2 have the same profile shapes (which is supported by our validation results), in first approximation, the AMFs of HONO and NO_2 are the same (equation (1)). We can therefore formulate RHN independently of the error-prone AMFs:

$$\mathrm{RHN} = \mathrm{VCD}_{\mathrm{HONO}}/\mathrm{VCD}_{\mathrm{NO_2,corr}} \approx \mathrm{SCD}_{\mathrm{HONO}}/\mathrm{SCD}_{\mathrm{NO_2,corr}} \qquad (2)$$

where $\mathrm{SCD}_{\mathrm{HONO}}$ is the HONO SCD, $\mathrm{SCD}_{\mathrm{NO_2,corr}} = \mathrm{SCD}_{\mathrm{NO_2}} - \mathrm{SCD}_{\mathrm{NO_2,strato}}$ is the retrieved NO_2 SCD ($\mathrm{SCD}_{\mathrm{NO_2}}$) corrected for its stratospheric contribution ($\mathrm{SCD}_{\mathrm{NO_2,strato}}$). An error budget on the SCDs and RHN is given in Supplementary Table 1. In particular, the estimated RHN error from the imperfect cancellation of AMFs (due to wavelength dependence) is less than ~1%.

To identify global HONO plumes and study source regions in a systematic and consistent way, a set of criteria was formulated that can be satisfactorily applied globally without the need for external fire data sources. Cloud information is not used either as it could lead to a statistical bias, for example, by filtering pyrocumulus clouds. After removing obvious outliers (based on fitting residuals), a detection test was applied: first, only satellite data over land were considered. Second, satellite data were kept when $\mathrm{SCD}_{\mathrm{HONO}} > 3\times\mathrm{SCDE}_{\mathrm{HONO}}$ (where $\mathrm{SCDE}_{\mathrm{HONO}}$ is the HONO SCD uncertainty from the fit) and if at least one neighbouring pixel satisfied the same criterion. An additional selection of the pixels with $\mathrm{SCD}_{\mathrm{NO_2,corr}} > 3\times\mathrm{SCDE}_{\mathrm{NO_2}}$ (where $\mathrm{SCD}_{\mathrm{NO_2}}$ is the NO_2 SCD uncertainty from the fit) was also applied to improve the selectivity of wildfire plumes and to stabilize RHN. However, the resulting pixel selection led to elevated false HONO detections over regions with a large anthropogenic NO_2 signal. Therefore, a final and conservative selection criterion on $\mathrm{SCD}_{\mathrm{HONO}} > 4\times10^{15}$ molecules cm^{-2} was used to retain only unambiguous pyrogenic HONO detections. Applying these rather strict criteria to one year of TROPOMI data yielded a set of 5,093 usable HONO ground pixel detections, all located over BB areas, which gives additional confidence in the selection approach.

Aircraft measurements. The BB-FLUX field campaign[68] took place during the summer of 2018 wildfire season in the Pacific Northwest around Boise. The University of Wyoming King Air research aircraft was equipped with remote sensing and in situ instruments, which included the University of Colorado Zenith Sky DOAS (CU ZS-DOAS) instrument, which performed measurements of NO_2, HONO, HCHO and CHOCHO using scattered solar photons in the zenith geometry. The aircraft was deployed underneath, inside and above the wildfire plumes to measure column enhancements, wind speed and plume vertical structure. HONO and NO_2 differential SCDs were retrieved using the same fit settings as TROPOMI (Supplementary Table 3). The background on either side of the plume was linearly interpolated and subtracted to derive trace gas SCD enhancements inside the plume. A total of 37 RFs were conducted, which studied wildfires in Idaho, California, Oregon, Nevada, Utah and Washington. A small subset of the BB-FLUX flights were actively coordinated to locate the plane below and/or near wildfire plumes at the TROPOMI overpass times. In particular, BB-FLUX RF11 on 12 August 2018 targeted the Rabbit Foot Fire in central Idaho close in time to the TROPOMI overpass (~20:45 UTC). The aircraft conducted two plume underpasses between 20:00 and 20:15 UTC 50 km downwind of the fire. Two additional flights were used for comparison with TROPOMI, BB-FLUX RF13 on 15 August 2018 (Rabbit Foot Fire) and BB-FLUX RF15 on 19 August 2019 (Watson Creek Fire, Oregon). For the two flights, the aircraft traverses sampled the wildfire plume at the TROPOMI overpass time ±15 min.

Although the satellite and aircraft HONO SCDs presented in this study agree well qualitatively, a thorough comparison is not straightforward because of differences in the spatial–temporal sampling of the air masses sounded by the two instruments, which have very different fields of view. Furthermore, the different observation geometries mean the retrievals have different sensitivity (light penetration) in the respective atmospheric vertical layers, in particular for large aerosol optical depths. We estimated this effect using the radiative transfer model LIDORT[48] version 2.7. A set of AMFs were calculated at a wavelength of 355 nm for typical BB plumes. As HONO (or NO_2) and aerosols are co-emitted, their vertical profiles were assumed to have the same shape modelled by a Gaussian peaking at 2 km above the surface, with a full-width at half-maximum of 0.5 km. BB aerosols were represented by a bimodal log-normal particle size distribution[49], with a single scattering albedo between 0.8 and 0.9, indicative of fresh to aged BB aerosols. Supplementary Fig. 3 shows an example of the dependence of the AMFs with aerosol optical depths. It illustrates the expected change in measurement sensitivity due to aerosols[50] and the inherent differences of AMF between aircraft and satellite measurements.

To evaluate the TROPOMI RHN estimates, we calculated RHN from the aircraft HONO and NO_2 SCDs data, for NO_2 background-corrected SCDs larger than 5×10^{15} molecules cm^{-2}. An error analysis of SCDs and RHN is given in Supplementary Table 1. The advantages of comparing RHNs are that they do not vary with the AMFs, and that RHN is independent of the horizontal resolution. However, a time difference exists between the aircraft and TROPOMI measurements (30–45 min in the case of RF11, and less than 15 min for RF13 and RF15), and a time adjustment is needed when the aircraft and satellite RHNs are compared. For this, we estimated the age of the plume separately for the aircraft and TROPOMI measurements, using trajectory calculations made with the FLEXPART-WRF[51] model. The Global Fire Assimilation System of the Copernicus Atmosphere Monitoring Service[52] was used for fire locations, plume injection heights and emitted amounts. We released around 1×10^5 'particles' from each fire location and followed each particle on its path through the atmosphere, tracking the time since its release. Processes like turbulence were allowed to act stochastically on each particle to modify its trajectory. Our dispersion calculations resulted in plume age spectra for each model grid box, which we then sampled along the flight path of the aircraft and the locations of the TROPOMI measurements. The mass-weighted mean of the age spectrum was used as a best guess for plume age; its standard deviation allowed us to identify contamination by the Goldstone fire downwind (Fig. 2), and the corresponding data were removed from the analysis. At the edges of the plume, the estimated plume age was sometimes found unrealistic due to very low particle concentrations, and the respective data were not considered in the comparison. In total, seven TROPOMI pixels (out of 40) were filtered to produce Fig. 2c.

Calculation of OH production rates. The OH production rates were calculated for every TROPOMI pixel in which HONO was detected, using model-estimated photolysis rates. The sources of OH considered include the photolysis of HONO, O_3 and oxygenated VOCs, and the ozonolysis of alkenes. The HONO, HCHO and CHOCHO mixing ratios were based on TROPOMI retrievals, whereas the concentrations of other VOCs were estimated from TROPOMI-derived HCHO and enhancement ratios (Δ(VOC)/Δ(HCHO)) based on field data. The calculation of concentrations requires assumptions on vertical profiles of the constituents and AMFs (see below). As these parameters are very uncertain (Supplementary Fig. 3), large uncertainties in OH production rates are expected; however, these assumptions have little impact on the relative contribution of HONO to the

total OH production rate presented here, as the vertical profiles of HONO and pyrogenic VOCs are expected to be very similar in the BB plumes.

The concentrations of HONO, HCHO and CHOCHO at the assumed peak altitude of 2 km were estimated from TROPOMI measurements of these compounds using the fixed vertical profile described above. The corresponding HCHO and CHOCHO SCDs (see examples in Supplementary Fig. 1) are extracted from the TROPOMI HCHO offline product[43] and the scientific CHOCHO product (adapted from GOME-2 (Global Ozone Monitoring Experiment–2) CHOCHO retrievals[53]). Details on the DOAS settings are provided in Supplementary Table 3. The calculations were performed for an assumed AMF of 0.5 for HONO and HCHO. An AMF of 1 was used for CHOCHO as radiative transfer test simulations (described above) demonstrated twice the measurement sensitivity in the visible part of the spectrum (where CHOCHO is retrieved) than that in the ultraviolet part. The estimated uncertainty of HCHO concentrations (relative to those of HONO) is ~27%, which results from an SCD uncertainty[43] of 10% and AMF errors related to differences in vertical profiles (20%) and in wavelength ranges of the retrievals (15%), based on radiative transfer model sensitivity calculations. The CHOCHO concentration uncertainty (30%) was assumed to be similar to that of HCHO.

The photolysis rates were obtained from the MAGRITTE (Model of Atmospheric Composition at Global and Regional Scales using Inversion Techniques for Trace Gas Emissions) chemistry-transport model[54,55], which relies on the TUV (tropospheric ultraviolet visible) photorate calculation package[56] with meteorological and other fields (pressure, temperature, surface downward solar radiation and total O_3 columns) derived from ECMWF (European Centre for Medium-Range Weather Forecasts) ERA-Interim reanalyses[57]. Potential misrepresentation of the effects of clouds and aerosols might lead to substantial uncertainties in the photorates, but with little influence on their relative magnitudes and therefore on the relative contributions of the different photolytic processes. The uncertainty of the relative contribution of non-photolytic processes (alkene ozonolysis) is increased due to these effects, by an assumed factor of 2, with very little impact on the overall uncertainty of HONO contribution.

A constant O_3 mixing ratio of 50 ppbv was assumed, whereas H_2O and temperature were obtained from ECMWF. Uncertainties in O_3 and H_2O are important but have little bearing on the conclusions, as O_3 photolysis and alkene ozonolysis contribute only a few percent to the total OH source.

Besides OH formation due to HONO and O_3 photolysis, the photolysis of organic compounds (primarily carbonyls) and the ozonolysis of alkenes generate OH radicals as well as HO_2 and RO_2 radicals, which are partially converted into OH, depending on the photochemical conditions[37]. BB plumes are usually characterized by high NO_x levels, in the ppbv range[58]. In the TROPOMI pixels in which HONO was detected and quantified, the estimated median NO_2 volume mixing ratio was ~25 ppbv at the peak of the plume, when an AMF of 0.5 was assumed. Adopting an NO/NO_2 ratio of 0.2, based on airborne measurements in BB plumes during the ARCTAS (Arctic Research of the Composition of the Troposphere from Aircraft and Satellites) campaign over boreal forests[59,60], the resulting NO concentrations (~5 ppbv) were such that HO_2 radicals produced in the plume were almost completely (>99%) converted into OH. The same applies to non-acyl RO_2 radicals, converted into HO_2 and then OH. For acylperoxy (ACO3) radicals, however, the formation of peroxyacetyl nitrate-like compounds through $ACO3 + NO_2$ is dominant, and only ~30% of these radicals are converted to OH, based on reported rates[61] for ACO3 + NO and $ACO3 + NO_2$ (for lower tropospheric conditions and $NO/NO_2 = 0.2$).

The VOC photolysis processes considered here are listed in Supplementary Table 4 along with their corresponding OH yield, which assume conversion efficiencies of 100% for HO_2 and non-acyl peroxy radicals, and 30% for ACO3 radicals. These yields are based on the Master Chemical Mechanism[62,63] (MCM) v3.3.1. The photorates (relative to that of HCHO) were estimated using TUV, with photolysis parameters from MCM. For furfural, the OH yield was assumed, and the photorate was calculated using published absorption cross-sections[64] and a quantum yield[65] of 0.01, of the same order as that of methacrolein and methylvinylketone[66].

The alkene ozonolysis processes considered are listed in Supplementary Table 5 along with their reaction rate and estimated OH yield, under the same assumptions as above. The reaction rates and products were obtained from MCM v3.3.1. Monoterpenes are speciated as 25% α-pinene and 75% β-pinene based on measurements in BB plumes during ARCTAS[59]. Supplementary Table 5 also provides the estimated OH production due to the reaction ($P_{OH}(VOC + O_3)$) for a given amount of the VOC (1 ppbv) and 50 ppbv O_3.

As noted above, HCHO and CHOCHO concentrations were constrained by TROPOMI observations. The concentrations of the other pyrogenic VOCs were estimated using VOC/HCHO enhancement ratios (Supplementary Table 6) obtained from the review of emission factors[10]. The enhancement ratio of two compounds is defined as the ratio of the excess concentrations of the two compounds in the fire plume relative to their ambient background concentrations. Enhancement ratios relative to CO or CO_2 are routinely used to estimate BB emission factors[8] ($g\,kg^{-1}$ dry matter). Here the molar enhancement ratios relative to HCHO were calculated as $ER(VOC) = (EF(VOC)/MW_{VOC})/(EF(HCHO)/MW_{HCHO})$, where EF denotes the emission factor ($g\,kg^{-1}$) and MW denotes molecular weight ($g\,mol^{-1}$). Note that the natural variability of emission rates and the role of secondary chemistry (chemical production and losses within the plume) imply a large variability of enhancement ratios; in particular, the ratios depend on plume age and photochemical conditions. Furthermore, many minor oxygenated VOCs are either not measured or have so far unknown impacts due to the lack of mechanistic information (for example, furfurals).

Supplementary Table 7 gives the estimated contributions of VOC photolysis reactions to the production of OH relative to the contribution of HCHO, as well as their estimated uncertainties. Those relative contributions are calculated as:

$$P_{OH}(VOC)/P_{OH}(HCHO) = (\Delta VOC/\Delta HCHO) \times J_{VOC}/J_{HCHO} \times Y_{OH}(VOC)/Y_{OH}(HCHO) \quad (3)$$

where the enhancement ratios (ΔVOC/ΔHCHO) are given in Supplementary Table 6, and photolysis rates (J) and OH yields (Y_{OH}) are given in Supplementary Table 5. Although there is some variation between VOC enhancement ratios according to fire type (extratropical forest, temperate forest, tropical forest and savanna), the combined contribution of all VOC + $h\nu$ reactions (besides HCHO + $h\nu$) is relatively uniform across fire types, and is of the same order as that of HCHO. When the contributions of HCHO and CHOCHO are excluded, the contribution of VOC + $h\nu$ can be approximated as 75 ± 66% of the HCHO + $h\nu$ contribution. The main contributing species are, besides HCHO and CHOCHO, methylglyoxal and biacetyl. Each of those two compounds contributes ~15–40% relative to that of formaldehyde.

Supplementary Table 8 provides the contribution of alkene ozonolysis to OH production for given levels of O_3 and HCHO in the plume, calculated as the product of the enhancement ratio (Supplementary Table 6) by P_{OH} (Supplementary Table 5). The total production of OH due to alkene ozonolysis is highest for temperate and boreal forest fires, due to their high emissions of monoterpenes. Based on these results, in the calculation of the overall OH production rate, the OH production rate per ppbv of HCHO was taken equal to 23 ± 17 pptv h^{-1} in tropical regions and 42 ± 62 pptv h^{-1} elsewhere.

Modelled global impact of pyrogenic HONO. MAGRITTE v1.1[55] was run at a 1° × 1° resolution to estimate the impact of pyrogenic HONO on global composition during summer 2018. The meteorology was obtained from ECMWF ERA-Interim. The model includes a detailed representation of biogenic and pyrogenic VOC oxidation[55,67]. The photolysis rate calculation relies on TUV, with daily aerosol optical depth distributions from CAMS (https://ads.atmosphere.copernicus.eu). BB emissions were calculated based on GFED4[32] with emission factors from a recent assessment[10].

Two 6-month runs (March–August) were conducted, with and without pyrogenic HONO. Gas-phase HONO formation and loss were included in both simulations. The pyrogenic HONO emission factors were 1.10, 1.36 and 2.29 $g\,kg^{-1}$ dry matter for savanna, tropical forest and extratropical forest fires, respectively, based on the RHN from Table 1 and NO_x emission factors[10], the NO/NO_2 ratio being taken as equal to 0.2 (see above).

Data availability

The global data and validation data that support the findings of this study are available in the BIRA-IASB Data Repository (http://repository.aeronomie.be) with the identifier https://doi.org/10.18758/71021058. The TROPOMI HONO dataset used in this study is also available from the corresponding author upon request. The BB-FLUX dataset is also available on request[68]. http://flights.uwyo.edu/projects/bbflux18/ Source data are provided with this paper.

Code availability

The DOAS code used to generate the satellite and aircraft data can be accessed at http://uv-vis.aeronomie.be/software/QDOAS/index.php. The chemical mechanism of the MAGRITTE model used in this study can be obtained at https://tropo.aeronomie.be/index.php/models/magritte.

References

40. Veefkind, J. P. et al. TROPOMI on the ESA Sentinel-5 Precursor: A GMES mission for global observations of the atmospheric composition for climate, air quality and ozone layer applications. *Remote Sens. Environ.* **120**, 70–83 (2012).
41. Levelt, P. F. et al. The ozone monitoring instrument. *IEEE Trans. Geosci. Remote Sens.* **44**, 1093–1101 (2006).
42. Bovensmann, H. et al. SCIAMACHY: mission objectives and measurement modes. *J. Atmos. Sci.* **56**, 127–150 (1999).
43. De Smedt, I. et al. Algorithm theoretical baseline for formaldehyde retrievals from S5P TROPOMI and from the QA4ECV project. *Atmos. Meas. Tech.* **11**, 2395–2426 (2018).
44. Wang, Y. et al. MAX-DOAS measurements of HONO slant column densities during the MAD-CAT campaign: inter-comparison, sensitivity studies on spectral analysis settings, and error budget. *Atmos. Meas. Tech.* **10**, 3719–3742 (2017).

45. Behrens, L. K. et al. GOME-2A retrievals of tropospheric NO_2 in different spectral ranges—influence of penetration depth. *Atmos. Meas. Tech.* **11**, 2769–2795 (2018).
46. Richter, A. & Burrows, J. P. Retrieval of tropospheric NO_2 from GOME measurements. *Adv. Space Res.* **29**, 1673–1683 (2002).
47. Palmer, P. I. et al. Air mass factor formulation for spectroscopic measurements from satellites: application to formaldehyde retrievals from the Global Ozone Monitoring Experiment. *J. Geophys. Res.* **106**, 14539–14550 (2001).
48. Spurr, R. J. VLIDORT: a linearized pseudo-spherical vector discrete ordinate radiative transfer code for forward model and retrieval studies in multilayer multiple scattering media. *J. Quant. Spectrosc. Rad.* **102**, 316–342 (2006).
49. Wang, P., Tuinder, O. N. E., Tilstra, L. G., de Graaf, M. & Stammes, P. Interpretation of FRESCO cloud retrievals in case of absorbing aerosol events. *Atmos. Chem. Phys.* **12**, 9057–9077 (2012).
50. Leitão, J. et al. On the improvement of NO_2 satellite retrievals—aerosol impact on the airmass factors. *Atmos. Meas. Tech.* **3**, 475–493 (2010).
51. Brioude, J. et al. The Lagrangian particle dispersion model FLEXPART-WRF version 3.1. *Geosci. Model Dev.* **6**, 1889–1904 (2013).
52. Kaiser, J. W. et al. Biomass burning emissions estimated with a global fire assimilation system based on observed fire radiative power. *Biogeosciences* **9**, 527–554 (2012).
53. Lerot, C., Stavrakou, T., De Smedt, I., Müller, J.-F. & Van Roozendael, M. Glyoxal vertical columns from GOME-2 backscattered light measurements and comparisons with a global model. *Atmos. Chem. Phys.* **10**, 12059–12072 (2010).
54. Stavrakou, T. et al. Impact of short-term climate variability on volatile organic compounds emissions assessed using OMI satellite formaldehyde observations. *Geophys. Res. Lett.* **45**, 1621–1629 (2018).
55. Müller, J.-F., Stavrakou, T. & Peeters, J. Chemistry and deposition in the Model of Atmospheric composition at Global and Regional scales using Inversion Techniques for Trace gas Emissions (MAGRITTEv1.0)—Part 1: chemical mechanism. *Geosci. Model Dev.* **12**, 2307–2356 (2019).
56. Madronich, S. in *Environmental Effects of Ultraviolet Radiation* (ed. Tevini, M.) 17–69 (Lewis, 1993).
57. Dee, D. P. et al. The ERA-Interim reanalysis: configuration and performance of the data assimilation system. *Q. J. R. Meteorol. Soc.* **137**, 553–597 (2011).
58. Trentmann, J., Andreae, M. O. & Graf, H.-F. Chemical processes in a young biomass-burning plume. *J. Geophys. Res.* **108**, 4705 (2003).
59. Jacob, D. J. et al. The Arctic Research of the Composition of the Troposphere from Aircraft and Satellites (ARCTAS) mission: design, execution, and first results. *Atmos. Chem. Phys.* **10**, 5191–5212 (2010).
60. Simpson, I. J. et al. Boreal forest fire emissions in fresh Canadian smoke plumes: C1–C10 volatile organic compounds (VOCs), CO_2, CO, NO_2, NO, HCN and CH_3CN. *Atmos. Chem. Phys.* **11**, 6445–6463 (2011).
61. Atkinson, R. et al. Evaluated kinetic and photochemical data for atmospheric chemistry: volume II—gas phase reactions of organic species. *Atmos. Chem. Phys.* **6**, 3625–4055 (2006).
62. Saunders, S. M., Jenkin, M. E., Derwent, R. G. & Pilling, M. J. Protocol for the development of the Master Chemical Mechanism, MCM v3 (Part A): tropospheric degradation of non-aromatic volatile organic compounds. *Atmos. Chem. Phys.* **3**, 161–180 (2003).
63. Jenkin, M. E., Young, J. C. & Rickard, A. R. The MCMv3.3. 1 degradation scheme for isoprene. *Atmos. Chem. Phys.* **15**, 11433–11459 (2015).
64. Colmenar, I. et al. UV absorption cross-sections between 290 and 280 of a series of furanaldehydes: estimation of their photolysis lifetimes. *Atmos. Environ.* **103**, 1–6 (2015).
65. Gandini, A., Parsons, J. M. & Back, R. A. The photochemistry of 2-furaldehyde vapour. II. Photodecomposition: direct photolysis at 253.7 and 313 nm and $Hg(^3P_1)$-sensitized decomposition. *Can. J. Chem.* **54**, 3095–3101 (1976).
66. Burkholder, J. B. et al. *Chemical Kinetics and Photochemical Data for Use in Atmospheric Studies* (Jet Propulsion Laboratory, 2015); http://jpldataeval.jpl.nasa.gov
67. Stavrakou, T. et al. Evaluating the performance of pyrogenic and biogenic emission inventories against one decade of space-based formaldehyde columns. *Atmos. Chem. Phys.* **9**, 1037–1060 (2009).
68. Volkamer, R. et al. *BB-FLUX: Biomass Burning Fluxes of Trace Gases and Aerosols* (University of Wyoming—Research Flight Center, 2019); http://flights.uwyo.edu/projects/bbflux18/

Acknowledgements

This work was performed in the frame of the TROPOMI and the BB-FLUX projects. We acknowledge financial support from ESA S5P MPC (4000117151/16/I-LG) and Belgium Prodex TRACE-S5P (PEA 4000105598) projects. The BB-FLUX project is supported by US National Science Foundation award AGS-1754019 (principal investigator, R.V.). C.F.L. received summer support from the Department of Chemistry, CU Boulder. H.F. is recipient of a NASA graduate fellowship. L.C. is a research associate supported by the Belgian FRS-FNRS. This paper contains modified Copernicus data (2018/2019) processed by BIRA-IASB. We thank T. Stavrakou for her advices on the model simulations. We acknowledge the open access policy of the GFED4 database. We thank the entire BB-FLUX science team, the pilots and the UW Flight Center staff. The plume age estimates contain modified Copernicus Atmosphere Monitoring Service Information 2019. Neither the European Commission nor ECMWF is responsible for any use that may be made of the information it contains. We acknowledge the use of imagery from the NASA Worldview application (https://worldview.earthdata.nasa.gov), part of the NASA Earth Observing System Data and Information System (EOSDIS). We acknowledge the use of data and imagery from LANCE FIRMS operated by NASA's Earth Science Data and Information System (ESDIS) with funding provided by NASA Headquarters.

Author contributions

N.T., R.V. and J.-F.M. designed the research, M.V.R. supervised the work. N.T, I.D.S., C.L., H.Y. and M.V.R. developed the satellite algorithms and processed the data. K.J.Z., N.K., H.F., T.K.K., C.F.L. and R.V. performed aircraft measurements and data analysis. J.-F.M. performed model calculations. C.K. performed plume age calculations. All the authors contributed to the text and interpretation of the results. N.T. analysed and interpreted the TROPOMI HONO data, with the help of R.V. and K.J.Z. N.T. prepared all the figures and wrote the manuscript, with input from all the co-authors.

Competing interests

The authors declare no competing interests.

Additional information

Extended data is available for this paper at https://doi.org/10.1038/s41561-020-0637-7.

Supplementary information is available for this paper at https://doi.org/10.1038/s41561-020-0637-7.

Correspondence and requests for materials should be addressed to N.T. or R.V.

Peer review information Primary handling editor: Clare Davis.

Reprints and permissions information is available at www.nature.com/reprints.

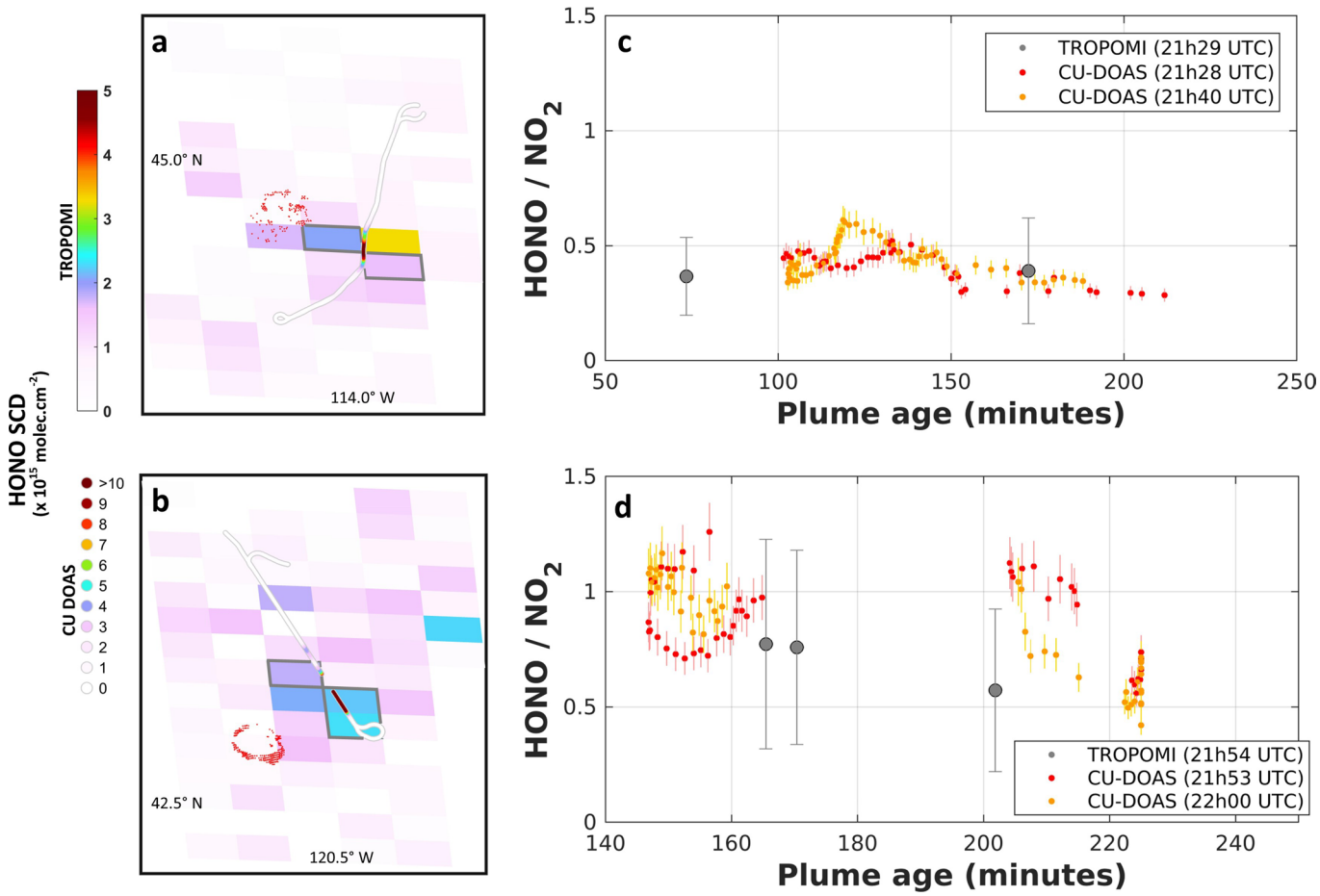

Extended Data Fig. 1 | Comparison between TROPOMI and aircraft (CU DOAS) measurements of the Rabbit Foot (Idaho) and Watson Creek (Oregon) fires on August 15 and 19, 2018. a, **b**, HONO slant columns from TROPOMI (rectangles) and nearly synchronized (± 15 minutes) aircraft CU-DOAS (dots), for Rabbit Foot fire (**a**) and Watson Creek fire (**b**). The fires source locations are indicated by the red points (source: https://firms.modaps.eosdis.nasa.gov/). **c**, **d**, Comparison between TROPOMI and aircraft RHN as function of plume age (Methods), respectively for (**a**, **b**). TROPOMI pixels delineated by grey lines in (**a**, **b**) are used for the comparison, and correspond to unambiguous detections of both HONO and NO_2 with SCDs>2xretrieval uncertainty (other pixels are considered not suitable for comparison). The two aircraft traverses of the plumes are plotted separately. Aircraft measurements more than 5 km away from the satellite pixels are not considered. Error bars correspond to systematic uncertainties on RHNs.

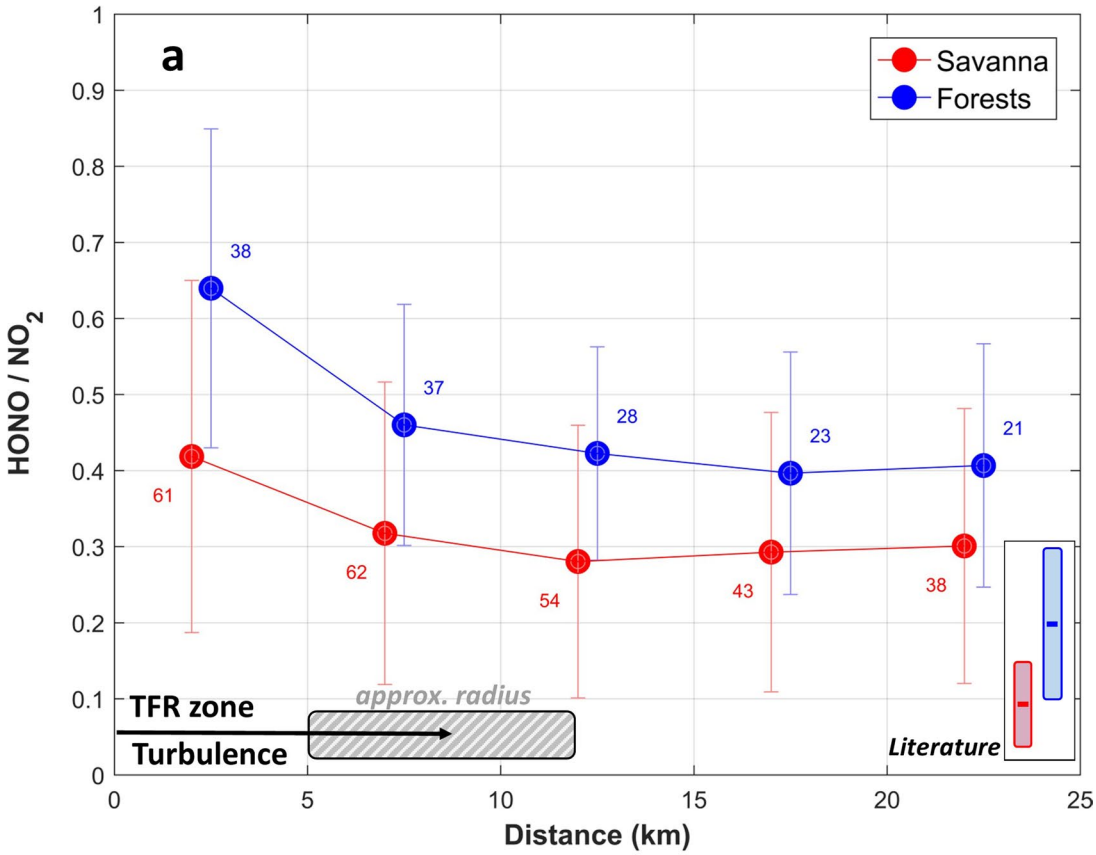

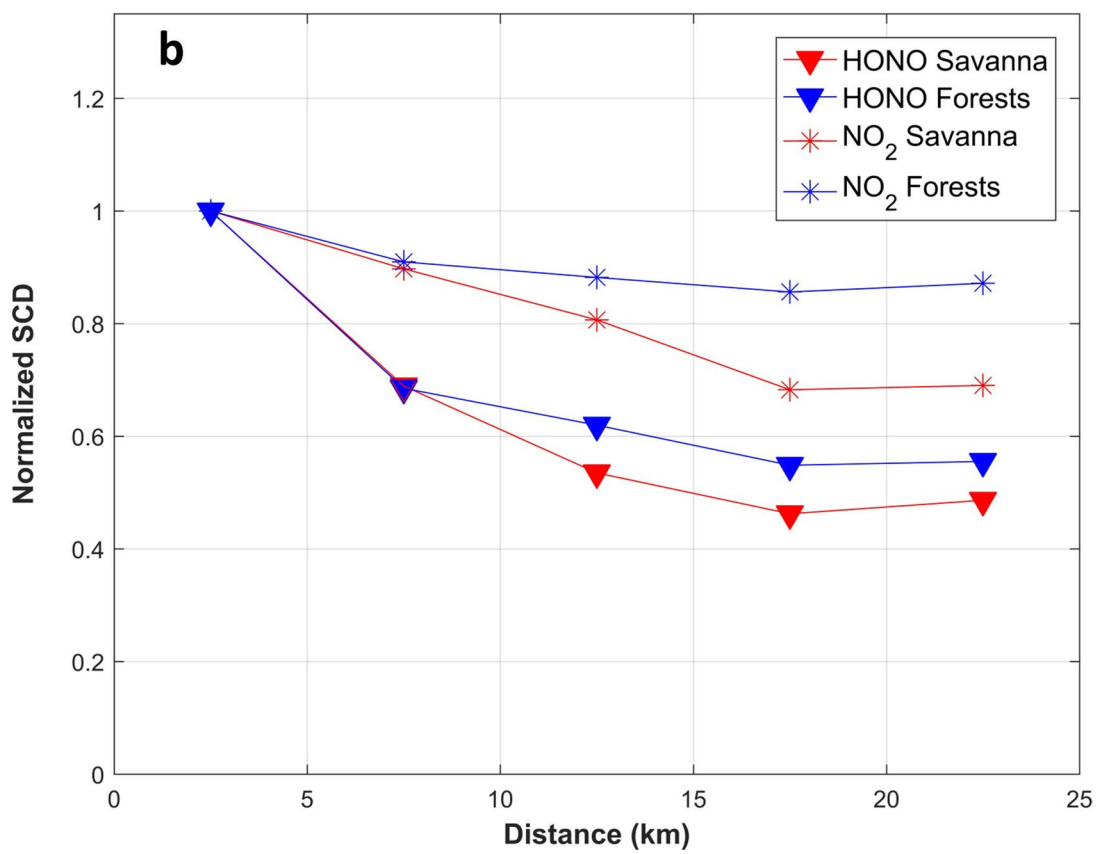

Extended Data Fig. 2 | See next page for caption.

Extended Data Fig. 2 | RHN and normalized slant columns dependence with distance from HONO maximum. a, Averages of RHN for extra-tropical forest and savanna ecosystems, as a function of the distance from the measured HONO maxima for the 100 largest measured HONO SCDs. Error bars are RHN standard deviations; numbers are the total pixels per distance bin. RHN peaks are found within the 5–12 km radius of temporary flight restriction (TFR) zone or affected by fire-induced turbulence. The TROPOMI results are classified using MODIS land cover type[39]. The inset colored bars indicate the range (mean ± standard deviation) of RHN found in the literature (Supplementary Table 2, excluding fresh plumes from large wildfires[34]). **b**, same as (**a**) for the HONO and NO_2 slant column densities (normalized).

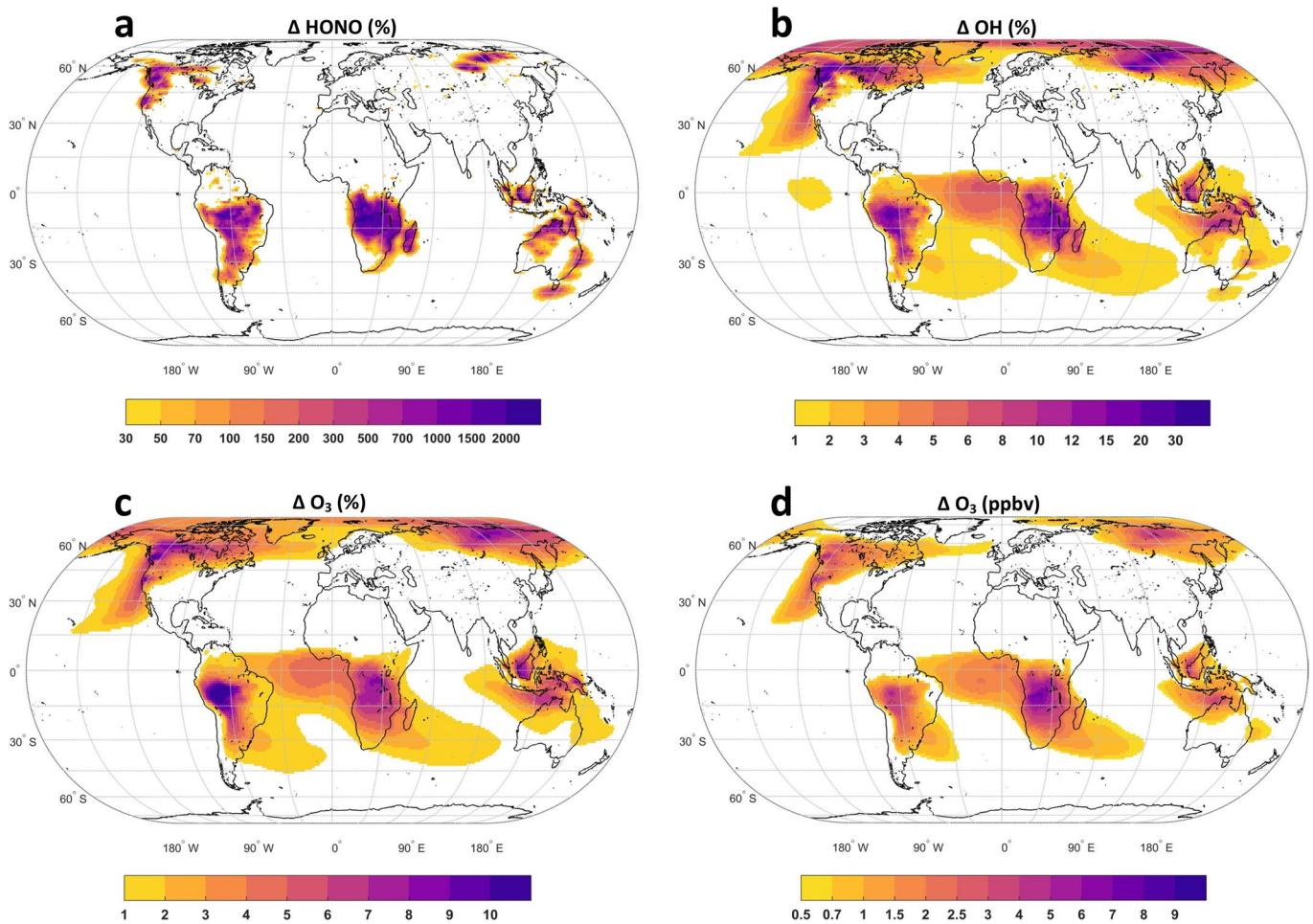

Extended Data Fig. 3 | Modelled impact of pyrogenic HONO. Calculated enhancement in the near-surface mixing ratios of HONO (**a**), OH (**b**) and O_3 (**c**, **d**) due to the inclusion of pyrogenic HONO emissions, for the month of August 2018.